Article

Surfactant-Assisted NiCo$_2$S$_4$ for Redox Supercapacitors

Mawuse Amedzo-Adore [ID] and Jeong-In Han *[ID]

Department of Chemical and Biochemical Engineering, Dongguk University, Seoul 04620, Republic of Korea;
mendeladore@dongguk.edu
* Correspondence: hanji@dongguk.edu

Abstract: Until now, crystalline NiCo$_2$S$_4$ and its composites have demonstrated improved performance in supercapacitor applications compared to their oxide analogues due to their relatively higher electrical conductivity and multifaceted redox reaction. However, amorphous phase materials have recently shown promise in electrochemical energy storage systems. This work reports on amorphous NiCo$_2$S$_4$ with the help of urea via the hydrothermal method. It was noted that urea not only aided the amorphous formation but also served as a nitrogen precursor. In comparison, amorphous NiCo$_2$S$_4$ demonstrated a higher nitrogen atom% of 5.9 compared to 4.49 for crystalline NiCo$_2$S$_4$. Furthermore, the amorphous NiCo$_2$S$_4$ electrode exhibited superior electrochemical performance, with a specific capacitance of ~3506 F g^{-1}, which was higher than the cNCS electrode's specific capacitance of ~2185 F g^{-1} at 2 A g^{-1}. Additionally, aNCS in a two-electrode asymmetric supercapacitor exhibited a specific capacitance and an energy density of ~196 F g^{-1} and 56 Wh kg^{-1}, respectively.

Keywords: NiCo$_2$S$_4$; binder free; amorphous; crystalline; supercapacitor; asymmetry

1. Introduction

Supercapacitors are known to possess a high power density, a long cycle life, and a quick charge–discharge cycle, and they are environmentally benign, hence their consideration as one of the electrochemical energy storage applications to tackle diminishing fossil fuel reserves as well as their environmental concerns [1,2]. Generally, two main categories of supercapacitors are known based on their energy storage mechanism: electrical double-layer capacitors (EDLCs), which involve non-faradaic reactions where charge adsorption/desorption occur via electrostatic interactions on the surface of the electrode, resulting in high rate performance and cycle stability, and pseudocapacitors, which involve charge storage through faradaic redox reactions within the bulk of the electrode [3,4]. Carbonaceous materials (activated carbon, nanotubes, and graphene), with their characteristic low cost, high conductivity, and large specific surface area, are widely used for EDLCs; however, they demonstrate a relatively low specific capacitance (~200 F g^{-1}), thereby limiting their practical applications [5]. In contrast, transition metal oxides and conductive polymers are materials commonly explored for pseudocapacitors and deliver relatively much higher capacitance than EDLCs. However, their poor electrical conductivity and framework swelling during cycling lead to low power density and cycle stability [6,7]. Therefore, the characteristics of electrode materials have a significant impact on the electrochemical performance of supercapacitors [8,9]. Hence, materials with the ability to utilize the synergistic properties of EDLCs and pseudocapacitors, hereafter referred to as hybrid supercapacitors, to give a higher capacitance with good rate and cycle performances have been explored [10].

To enhance the capacitance performance of materials, heteroatom (B, N, S) doping has been demonstrated as an effective strategy due to its ability to modify the surface of materials [5,11,12]. Notably, for nitrogen doping, it has been demonstrated that the presence of pyrrolic and pyridinic nitrogen, which serve as faradaic sites for pseudocapacitance, and graphitic nitrogen and pyridinic nitrogen oxide, which can enhance electrical

conductivity, are essential for enhancing the electrochemical performance of carbon-based materials [11–13]. It has been demonstrated that the presence of a high content of nitrogen provides a larger surface area, leading to high specific capacitance with excellent cycle stability [14,15]. Additionally, it has been shown, theoretically, that the low electronegativity of sulfur to oxygen enables the realization of a more flexible structure when oxygen is replaced by sulfur in a material [16]. Thus, transition metal sulfides with relatively higher electrical conductivity resulting from their lower band gap, which are essential for faster electron transport to enhance electrochemical performance, have received much interest in recent times [16–18]. Among transition metal sulfides, nickel–cobalt sulfides ($NiCo_2S_4$) have seen much interest in recent years for diverse applications, such as electrochemical water splitting, gas sensors, supercapacitors, and batteries [19,20]. Despite the promise shown by $NiCo_2S_4$ in supercapacitor applications, it suffers from surface oxidation in alkaline electrolytes and unsatisfactory cycle performance, which limit its practical applications [21]. To mitigate the challenges mentioned above, various approaches (composite with other materials, tuning the morphology, and varying elemental stoichiometry) have been employed to enhance the electrochemical performance of $NiCo_2S_4$ [22–26].

Conventionally, $NiCo_2S_4$ powder is obtained and mixed with conductive carbon and a low-conductive binder to form a slurry and subsequently coated on a current collector for electrochemical analysis. The electron transfer between the electrode material and the current collector might be hindered due to the change in electrical conductivity of the electrode induced by the binder, which limits the rate and cycle performance of the electrode [27]. To limit the side effects of the binder on the electrochemical performance of the electrode, the direct growth of material on a current collector, which is subsequently used as a binder-free electrode for electrochemical analysis in supercapacitor applications, has recently received much attention. Kulurumotlakatla et al. obtained hierarchical $NiCo_2S_4$ grown on nickel foam, which was employed as a binder-free electrode for supercapacitor applications. It demonstrated a specific capacity of ~154.13 mAh g^{-1} at 2 A g^{-1}, a high rate performance, and a capacity retention of 95.2% at 4 A g^{-1} after 5000 cycles [17]. Yang et al. obtained binder-free 3D-structured flaky arrays of $NiCo_2S_4$ on Ni foam through the sulfurization (anion exchange) of a $NiCo_2O_4$ nanorod. The electrode exhibited a high specific capacitance of 2044 F g^{-1} at 1 A g^{-1} and a capacitance retention of 77% after 2000 cycles [28]. Also, Wen et al. obtained binder-free Ni-Co-S with various Ni/Co ratios deposited on a carbon cloth, where it was demonstrated that the ratio of Ni/Co ions is essential in tuning the material's morphology. Here, the optimized electrode showed a specific capacitance of 640 F g^{-1}, with an 84% capacitance retention after 10,000 cycles and an energy density of 33.9 Wh kg^{-1} at a power density of 839 W kg^{-1} [29]. By varying the hydrothermal reaction time, Xue et al. obtained a composite of $NiCo_2S_4$ hollow nanotubes covered with NiMn-LDH nanosheets, with a controlled growth density. With its higher specific surface area and average pore diameter, the composite electrode demonstrated a superior specific capacity of 822.64 C g^{-1} at 50 mA cm^{-2}, with a 92.7% capacity retention after 5000 cycles and energy and power densities of 53.1 Wh kg^{-1} and 370.82 W kg^{-1}, respectively [30].

Recently, obtaining the amorphous phase of a material has been regarded as a crucial strategy for improving the electrochemical performance of electrode materials. The amorphous material is considered to possess more lattice defects than its corresponding crystalline phase, which can provide more active sites to facilitate electron transfer, leading to improved electrochemical properties [31,32]. For example, Sun et al. demonstrated that amorphous FeO_x nanosheets possess a larger interatomic distance and a looser packing than their crystalline counterparts, which resulted in an enhanced specific capacity of 263.4 mAh g^{-1} at 0.1 A g^{-1} after 100 cycles, as an anode electrode for a sodium-ion battery [33]. Additionally, Ren et al. demonstrated that amorphous cobalt sulfide with more defects and the absence of grain boundaries exhibited superior electrochemical properties as an anode in lithium-ion batteries [34]. By varying the reaction time, Zhou et al. also demonstrated tuning the phase of selenium from crystalline to amorphous phases.

With its higher specific surface area, amorphous selenium nanowire exhibited a superior storage capacity of 755 mAh g^{-1} than its corresponding crystalline phase [35].

In this report, the synthesis of amorphous and crystalline phases of NiCo$_2$S$_4$ grown on Ni foam were obtained via the hydrothermal method, and their electrochemical performance in supercapacitor applications was investigated. In this approach, the surfactant (urea) played a vital role in obtaining the desired phases (amorphous and crystalline), as well as introducing nitrogen doping into the material. The introduction of urea allows for nitrogen doping, which is essential for enhancing the electrochemical properties of the material. It was demonstrated that amorphous NiCo$_2$S$_4$ with higher nitrogen content exhibited superior electrochemical performance than its crystalline phase counterpart.

2. Materials and Methods

2.1. Chemicals

Nickel (II) nitrate hexahydrate (Ni(NO$_3$)$_2$·6H$_2$O, 99.99%, Aldrich, Seoul, Republic of Korea), cobalt (II) hexahydrate (Co(NO$_3$)$_2$·6H$_2$O, 97% Junsei), urea (CH$_4$N$_2$O, 98%, Sigma-Aldrich, Incheon, Republic of Korea), hexamethylenetetramine (HMTA, C$_6$H$_{12}$N$_4$, 99%, Sigma-Aldrich), sodium sulfide nanohydrate (Na$_2$S·9H$_2$O, 98%, Sigma-Aldrich), and activated carbon (AC, Sigma-Aldrich, Seoul, Republic of Korea) were purchased and used with no further purifications.

2.2. Material Synthesis

NiCo$_2$S$_4$ on nickel foam was synthesized using a modified synthesis method reported earlier [36]. Ni(NO$_3$)$_2$·6H$_2$O (1 mmol), Co(NO$_3$)$_2$·6H$_2$O (2 mmol), CH$_4$N$_2$O (8 mmol), and C$_6$H$_{12}$N$_4$ (6 mmol) were added sequentially to 50 mL of methanol, with continuous magnetic stirring for 30 min. Na$_2$S·9H$_2$O (4 mmol) was then added to the above solution and stirred for another 30 min. The homogeneous mixture formed was then transferred into a 100 mL Teflon-lined stainless steel autoclave. Subsequently, nickel foam (4.5 cm × 1.3 cm) was then immersed into the Teflon-containing solution, and hydrothermal synthesis was performed for 18 h at 180 °C. The nickel foam-supported material was removed from the cooled Teflon, washed several times with D.I. water and ethanol, and dried overnight at 60 °C to obtain the final product, henceforth referred to as aNCS. A control material was also synthesized using the above procedure, using only HMTA as the surfactant (without urea). The final product obtained is henceforth referred to as cNCS. The average loading mass of NCS on nickel foam was 1.2 mg.

2.3. Material Characterization

The materials' structural phases were determined by X-ray diffraction (XRD) using a laboratory Rigaku Ultima V diffractometer(Bruker AXS, Karlsruhe, Germany) with a Cu Kα radiation source. The morphology and elemental distribution of the materials were analyzed using field-emission scanning electron microscopy (FE-SEM, JOEL-7800F, Japan Electron Optics Laboratory, Tokyo, Japan) and high-resolution transmission electron microscopy (HR-TEM, JEM-2100Plus, Japan Electron Optics Laboratory, Tokyo, Japan). Using X-ray photoelectron spectroscopy (XPS, Perkin-Elmer PHI 1600 ESCA system, Thermo Scientific Inc., UK), the samples' elemental compositions were determined.

2.4. Electrochemical Test

The as-synthesized aNCS and cNCS were used as binder-free electrodes for supercapacitor applications. Using 3M KOH as the electrolyte, the electrodes' electrochemical characteristics, including cyclic voltammetry (CV), galvanostatic charge–discharge (GCD), and impedance spectroscopy (EIS), were measured in a three-electrode system (Biologic SP-150 workstation, BioLogic, Paris, France). The binder-free electrodes (aNCS and cNCS), Ag/AgCl electrode, and platinum wire were utilized as working, reference, and counter

electrodes, respectively. The specific capacitance was estimated based on the GCD profiles according to the following equation:

$$C = \frac{I \times \Delta t}{m \times \Delta V} \tag{1}$$

where C represents the specific capacitance (F g^{-1}), I defines the current (A), Δt refers to the discharge time (s), m represents the loading mass of active material (g), and ΔV refers to the potential window (V).

Additionally, a two-electrode asymmetric supercapacitor (ASC) system was also assembled and analyzed for the aNCS, where activated carbon (AC) was used as the counter electrode in a 3M KOH aqueous electrolyte.

3. Results and Discussion

X-ray diffraction (XRD) analysis was employed to ascertain the structural phases of the samples.

Figure 1a shows the XRD patterns of both samples, where both samples show diffraction peaks at ~45, 52, and 77 °C, which are assigned to Ni obtained from the Ni foam substrate. With further enlargement of the diffraction peaks of both materials (Figure 1b), diffraction peaks were observed for cNCS which match with the NiCo$_2$S$_4$ patterns reported previously [37]. However, for aNCS, there were no diffraction peaks, indicating an amorphous state of the sample. The role of urea in the formation of the amorphous phase was confirmed in Figure S1a,b, where an amorphous material was obtained when only urea was used as the surfactant. This indicates that the introduction of urea during synthesis is essential to obtain amorphous NiCo$_2$S$_4$. The morphologies of cNCS (Figure S1c) and aNCS (Figure 1c) demonstrate similar nanosheet shapes. However, aNCS appears to have smaller nanosheets than cNCS, which can be attributed to the decomposition of urea, leading to the release of NH$_4^+$ and CO$_3^{2-}$. The release of these gasses might have helped form smaller nanosheets, thereby providing a larger surface area for a higher capacitance. The corresponding TEM image of aNCS (Figure 1d) exhibited the interior structure of the samples, which agreed with the SEM images. The HRTEM of aNCS (Figure 1e) and its corresponding SAED pattern (insert: Figure 1e) show a diffused halo ring, which is characteristic of an amorphous phase, confirming that the aNCS material is amorphous, which is in agreement with the XRD analysis. However, the SAED pattern of cNCS (insert: Figure S1d) shows a characteristic crystalline phase. HAADF-STEM color mapping of aNCS (Figure 1) revealed an even distribution of the elements (Ni, Co, and S), confirming the elemental composition of the material.

Further confirmation of elemental composition and their chemical states were investigated by employing XPS analysis. Figure S2a presents the XPS spectra of both the cNCS and aNCS materials, showing the presence of Ni 2p, Co 2p, and S 2p. Additionally, it can be confirmed that both materials contain the same elements, as shown in Figure S2b–d. Additionally, the XPS spectra reveal the presence of nitrogen, which can be attributed to the surfactants (HMTA and urea) employed during synthesis. The N 1s spectra of both materials (Figure 2a) show the presence of three peaks at ~398.77–399.2, 402.5, and 406.3 eV, which are assigned to pyridinic nitrogen (N-6), graphic nitrogen (N-Q), and pyridine nitrogen oxide (N-O), respectively [5,13,38]. However, aNCS consists of a ~5.9 atom % of total nitrogen, which is higher than the ~4.49 atom % for cNCS. As shown in Table 1, where aNCS contains higher N-5 and N-O values, which are essential for enhancing electrical conductivity [39], the aNCS material is expected to exhibit superior electrochemical performance than that of the cNCS. This phenomenon confirmed that urea was not only responsible for the amorphous phase formation of NiCo$_2$S$_4$ on Ni foam but also that it served as the N-doping precursor.
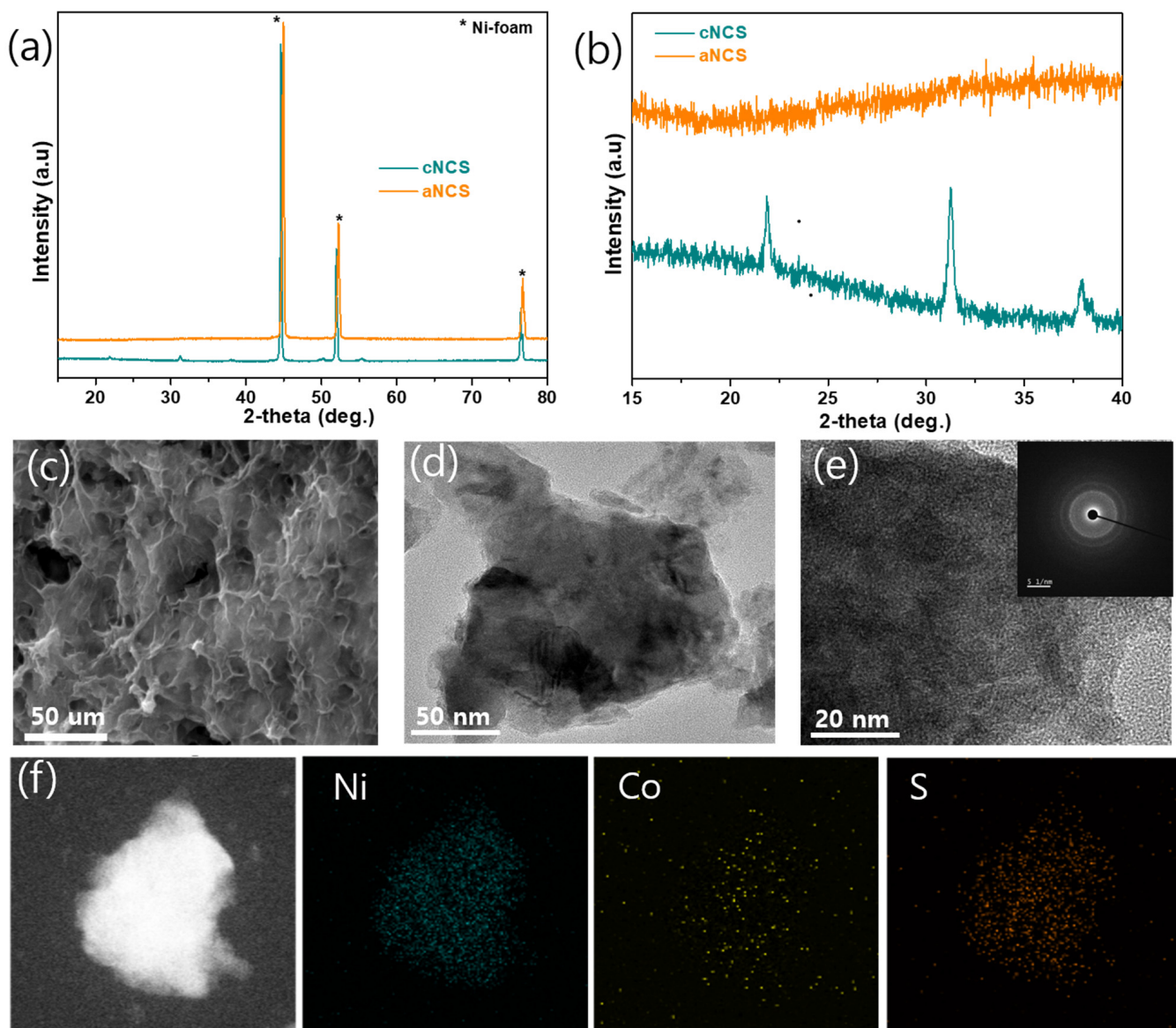
Figure 1. (**a**) XRD patterns and (**b**) enlarged XRD patterns of the cNCS and aNCS materials compared. (**c**) FESEM image, (**d**,**e**) HR-TEM images (insert: SAED pattern), and (**f**) HAADF-STEM image with corresponding elemental color mapping images of aNCS.

Furthermore, high-resolution XPS spectra of individual elements were obtained using the Gaussian fitting method (Figure 2b–d). The Ni 2p spectrum (Figure 2b) shows two characteristic peaks ascribed to Ni $2p_{3/2}$ (854.68 eV) and Ni $2p_{1/2}$ (872.46 eV), together with satellite peaks. Additionally, the deconvoluted spectra exhibited the presence of Ni^{2+} and Ni^{3+} [28]. Similarly, the Co 2p spectra (Figure 2c) also show two characteristic peaks assigned to Co $2p_{3/2}$ (780.23 eV) and Co $2p_{1/2}$ (795 eV) [40]. In Figure 2d, the S 2p spectra show characteristic peaks at 162.42 eV and 167.83 eV, which correspond to S $2p_{3/2}$ and S $2p_{1/2}$, respectively [41].

Additionally, the electrochemical properties of both materials (cNCS and aNCS) were examined in a three-electrode system, where the materials with no further treatment were employed as binder-free working electrodes. Figure 3a presents the CV profile comparison of the aNCS and cNCS electrodes in a potential window of 0.0–0.5 V at a scan rate of 10 mV s^{-1}, where both electrodes demonstrate similar distinct curves, which are characteristic of battery-type supercapacitors (diffusion-driven mechanism). This agrees

with the electrochemical reaction of $NiCo_2S_4$ in a KOH aqueous electrolyte [42] according to the following equations:
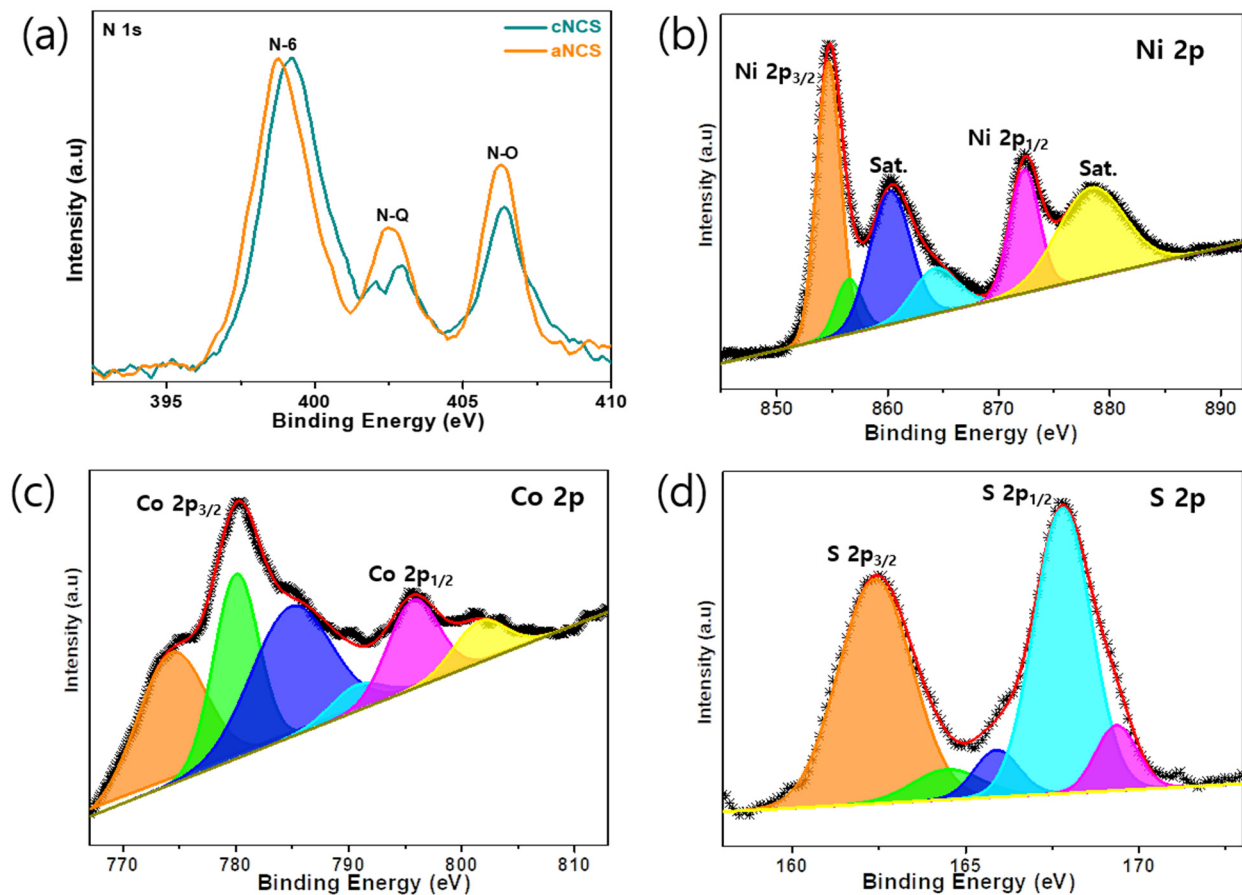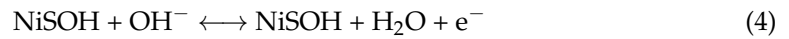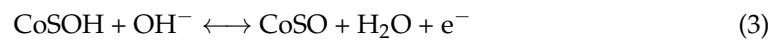
$$NiCo_2S_4 + 4OH^- \longleftrightarrow NiSOH + 2CoSOH + SOH^- + 3e^- \tag{2}$$

$$CoSOH + OH^- \longleftrightarrow CoSO + H_2O + e^- \tag{3}$$

$$NiSOH + OH^- \longleftrightarrow NiSOH + H_2O + e^- \tag{4}$$

Figure 2. (**a**) N 1s XPS spectra of the cNCS and aNCS samples compared. High-resolution XPS peaks of (**b**) Ni 2p, (**c**) Co 2p, and (**d**) S 2p from the aNCS sample.

Table 1. Summary of N atom content in samples.

Sample	N (atom %)	N-6 (atom %)	N-Q (atom %)	N-O (atom %)
cNCS	4.49	2.70	0.78	1.01
aNCS	5.90	3.22	1.22	1.46

However, the aNCS electrode exhibited a larger area, indicating that it possesses a relatively higher storage capacitance than the cNCS electrode. Figure 3b and Figure S3a are the CV profiles of aNCS and cNCS, respectively, at various scan rates (10–50 mV s^{-1}), which show similar redox peaks where the peak current areas increased with increasing scan rates. The GCD profiles of the electrodes measured at a current density of 2 A g^{-1} are shown in Figure 3c, where aNCS exhibited a larger discharge time of 874 s compared to cNCS with a discharge time of 545 s, which implies that the aNCS electrode possesses a higher specific capacitance than the cNCS electrode. The GCD profiles measured at various current densities (2–10 A g^{-1}) are shown in Figure 3d and Figure S3b for the aNCS and cNCS electrodes, respectively, which show excellent electrochemical redox

reversibility, demonstrated by their consistent symmetrical profiles with current density. The corresponding rate capability is shown in Figure 3e, where aNCS exhibited a superior rate performance, with specific capacitances of 3506 and 3168 F g^{-1} compared to 2185 and 1783 F g^{-1} for cNCS, at current densities of 2 and 10 A g^{-1}, respectively. The aNCS electrode also demonstrated superior cycle performance, with an initial capacitance retention of ~90% compared to ~84% for cNCS, at a current density of 10 Ag^{-1} after 5000 cycles.

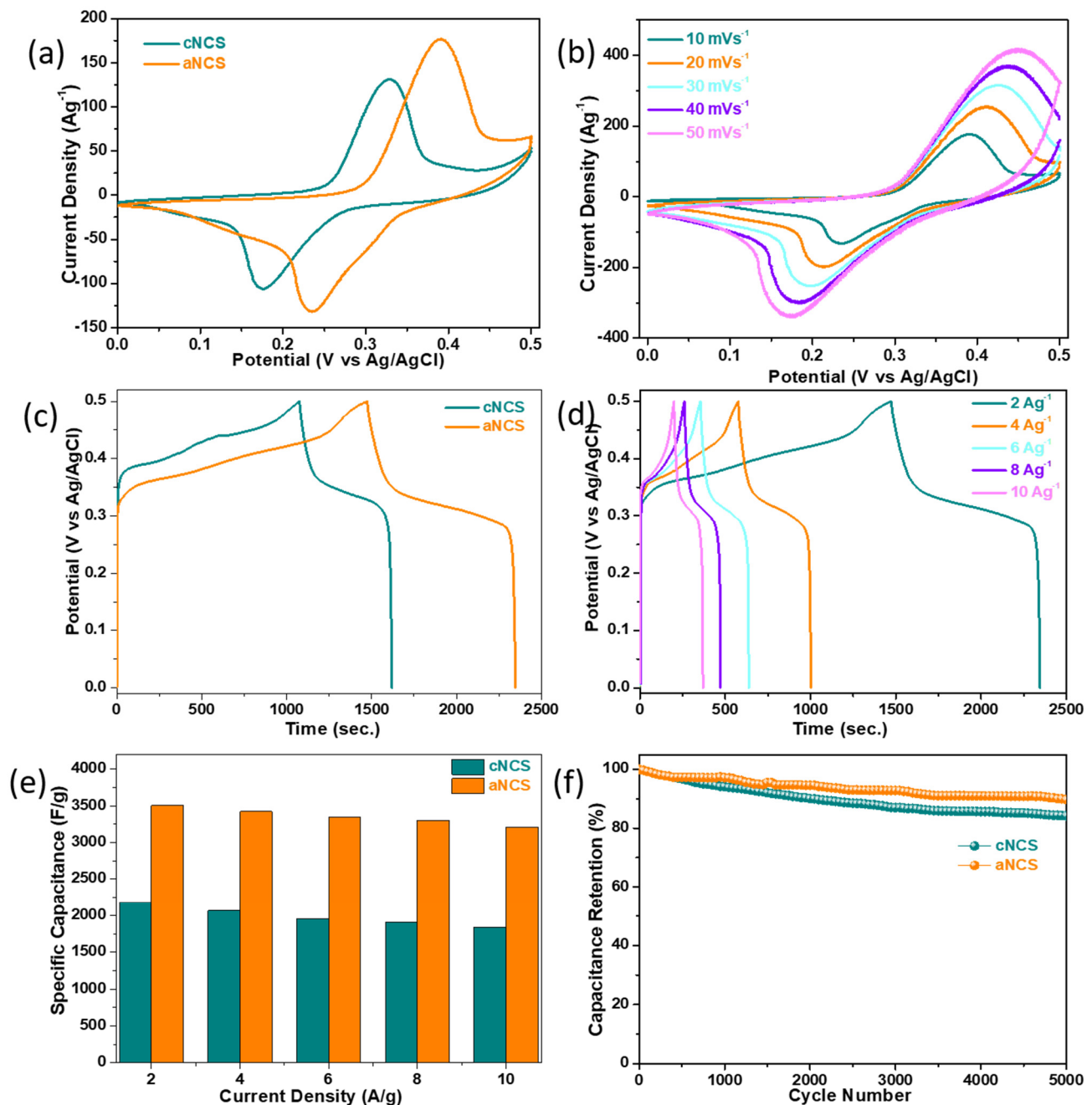**Figure 3.** (**a**) CV profiles of electrodes at 10 mV s^{-1}. (**b**) CV profiles of aNCS measured at various scan rates. (**c**) Comparison of GCD profiles of electrodes at 2 A g^{-1}. (**d**) GCD profiles of aNCS at various current densities. (**e**) Rate capability and (**f**) capacitance retention of electrodes measured at a current density of 10 A g^{-1}. All tests were conducted in a potential window 0–0.5 V.

The Ni foam's contribution to the materials' capacitance was negligible, as confirmed by the CV and GCD profiles of the Ni foam shown in Figure S4. The superior electrochemi-

cal performance exhibited by the aNCS electrode can be attributed to its higher nitrogen content. This provided a larger surface area and enhanced the electrical conductivity.

Furthermore, aNCS shows lower charge-transfer resistance than cNCS, as shown in Figure 4a, which implies faster charge transfer in aNCS, leading to enhanced electrochemical performance [43]. Using the power-law relationship [44], the so-called *b*-value was obtained from the CV profiles at various scan rates. From Figure 4b, *b*-values of 0.52 and 0.49 were obtained for aNCS and cNCS, respectively, which demonstrates that the electrochemical reaction of both electrodes is predominantly diffusion controlled. Additionally, by using Dunn's method [45,46], the contribution ratio of reaction mechanisms at various scan rates was computed (Figure 4c), where the electrode showed a 94% diffusion-driven mechanism at 20 mV s^{-1} (Figure 4d).
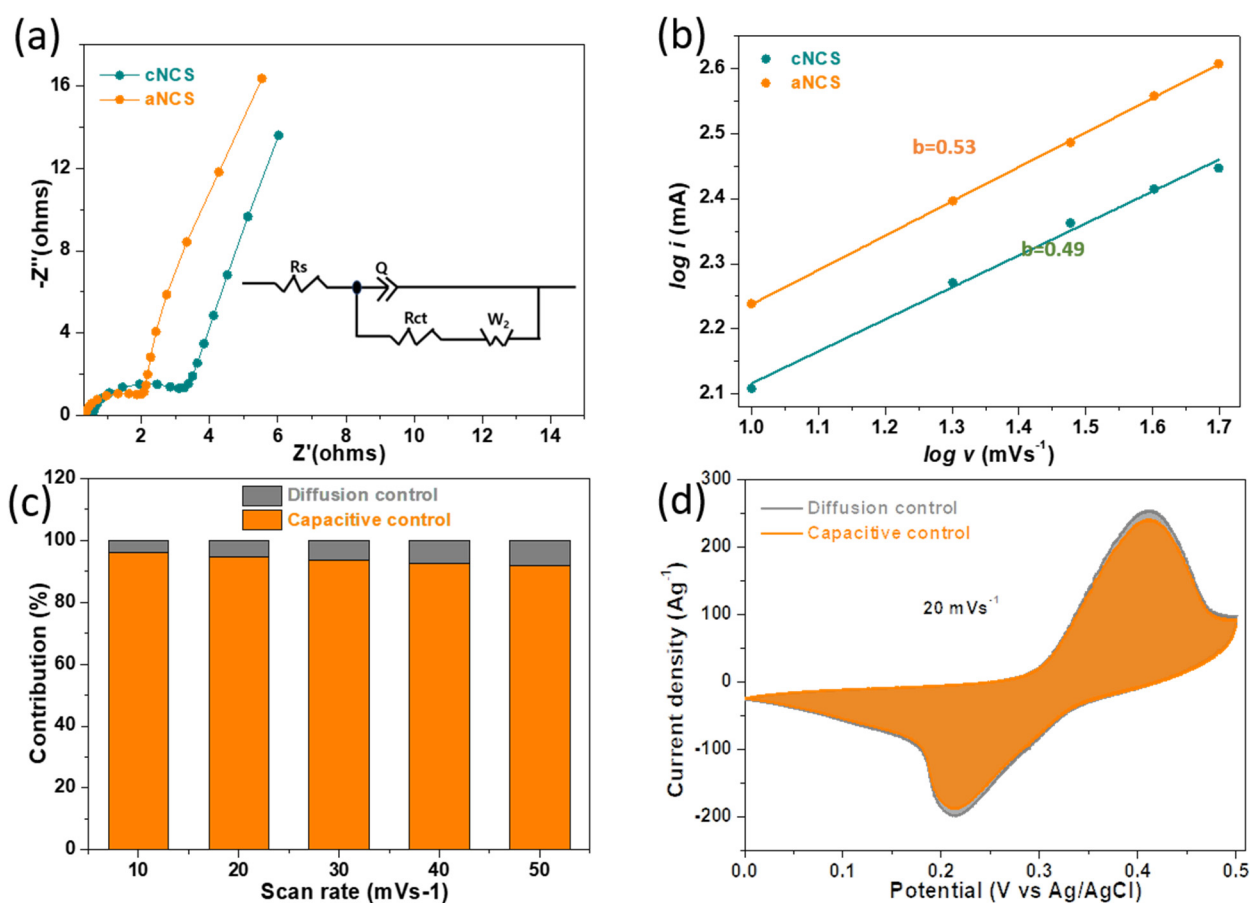

Figure 4. (**a**) Comparison of EIS plots of the electrodes. (**b**) Plot of log *v* against log *i*, obtained from CV profiles. (**c**) Contribution ratio of the surface-controlled mechanism to the capacitance of the aNCS electrode at different scan rates. (**d**) Contribution ratio of the surface-controlled mechanism to the capacitance at 20 mV s^{-1}.

For practical application, the aNCS electrode was used in a two-electrode asymmetric supercapacitor (ASC), with commercial activated carbon (AC) as the counter electrode. Figure S5 presents the CV and GCD profiles of the AC obtained using a three-electrode system in a potential window of −1.0–0.0 V in a 3M KOH electrolyte. The AC electrode exhibited typical, characteristic EDLC behavior with quasi-rectangular and triangular symmetrical shapes using CV and GCD, respectively. Figure 5a shows the non-overlapping CV profiles of the aNCS and AC electrodes at a scan rate of 10 mV s^{-1} obtained in a three-electrode system to help screen for the stable operating potential window of both electrodes [47].

The CV profiles of the ASC obtained at various scan rates in a potential window of 0–1.45 V are shown in Figure 5b, where the profiles demonstrated similar shape, suggesting

excellent rate performance. The GCD profiles (Figure 5c) and corresponding rate capability (Figure 5d) at various current densities (1–5 A g^{-1}) were obtained, where the electrode demonstrated capacitances of 196, 180, 165, 149, and 128 A g^{-1} at current densities of 1, 2, 3, 4, and 5 A g^{-1}, respectively. Additionally, the electrode demonstrated an excellent initial capacitance retention of ~92.4% at a current density of 10 A g^{-1} after 5000 cycles. The electrode also exhibited an energy density of 57 Wh kg^{-1} at a low power density of 960 Wk g^{-1}, as shown in Figure 5e. These excellent electrochemical performances exhibited by amorphous NCS were promising in comparison to previously reported work on NiCo$_2$S$_4$ and their composites, as shown in Table S1.
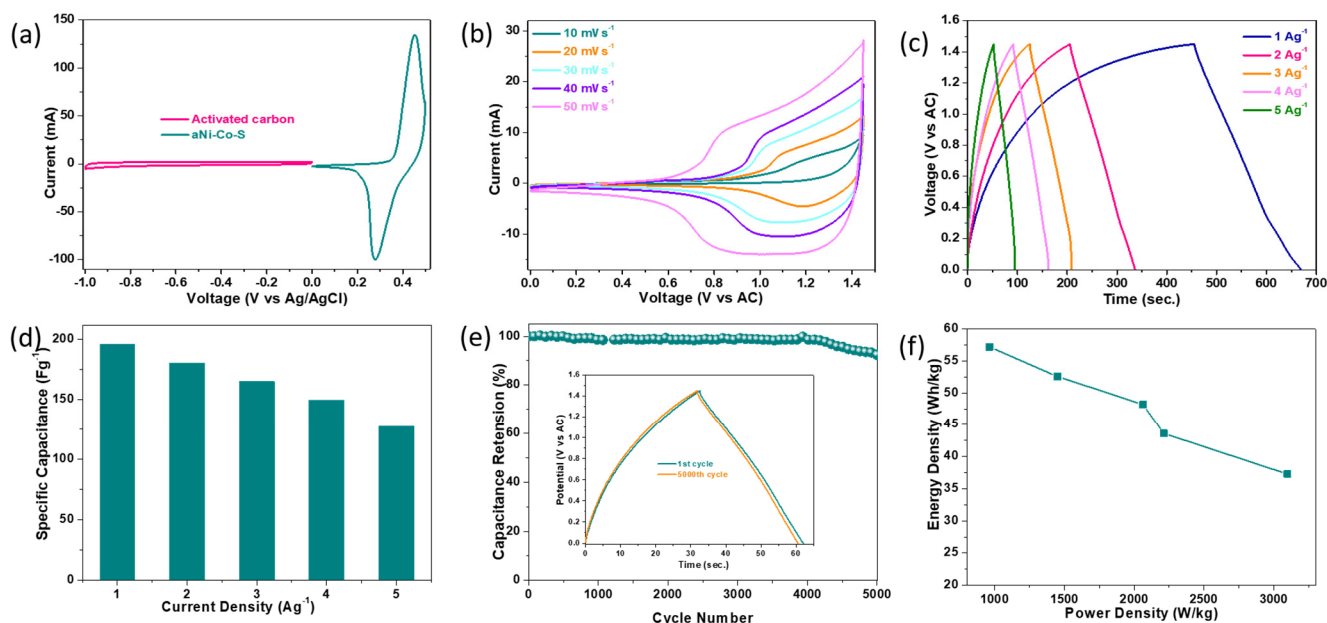

Figure 5. (**a**) CV profiles of the AC and aNCS electrodes measured in potential windows of −1.0–0.0 V and 0.0–0.5 V, respectively, at a scan rate of 20 mV s^{-1} in a three-electrode system. (**b**) CV profiles at various scan rates. (**c**) GCD profiles at various current densities. (**d**) Rate capability and (**e**) capacitance retention (insert: GCD profiles) at a current density of 10 A g^{-1}. (**f**) Plot of energy density against power density of the aNCS//AC asymmetric supercapacitor measured in a potential window of 0.0–1.45 V.

4. Conclusions

In summary, crystalline and amorphous NiCo$_2$S$_4$ on nickel foam were successfully synthesized using the hydrothermal method. During synthesis, the use of urea was vital to successfully obtain the desired phases (amorphous). Additionally, the use of urea also helped increase the nitrogen atom% content in the amorphous material, which is essential for increasing the conductivity of the material. When used as a binder-free working electrode in a three-electrode system with an aqueous electrolyte, aNCS demonstrated superior electrochemical performance, with a higher specific capacitance of 3506 F g^{-1} compared to 2185 F g^{-1} for cNCS at a current density of 2 A g^{-1}. Additionally, aNCS exhibited superior rate capability and cycle performance, with a 90% initial capacitance retention compared to an ~84% capacitance retention for cNCS after 5000 cycles at 10 A g^{-1}. The superior performance demonstrated by aNCS over cNCS can be attributed to the higher nitrogen atom% content caused by the introduction of urea, resulting in superior electron transfer. In a two-electrode asymmetric supercapacitor (ASC) system, the aNCS electrode demonstrated a specific capacitance of 196 F g^{-1} at a current density of 1 A g^{-1}. Additionally, the electrode exhibited high energy and power densities of 57 Wh kg^{-1} and 960 W kg^{-1}, respectively, as well as a ~92% initial capacitance retention after 5000 cycles.

Supplementary Materials: The following supporting information can be downloaded at https://www.mdpi.com/article/10.3390/batteries10100360/s1: Figure S1: XRD, SEM, and TEM images of cNCS; Figure S2: XPS spectrum and XPS spectra of Ni 2p, Co 2p, and S 2p of both cNCS and aNCS samples; Figure S3: CV and GCD profiles of cNCS electrode; Figure S4: CV and GCD profiles of bare Ni foam; Figure S5: CV and GCD profiles of commercial activated carbon; Table S1: Comparison of some reported supercapacitor performances of NiCo2S4-related electrodes.

Author Contributions: Conceptualization, M.A.-A.; methodology, M.A.-A.; investigation, M.A.-A.; data curation, M.A.-A.; writing—original draft preparation, M.A.-A.; writing—review and editing, J.-I.H.; supervision, J.-I.H.; funding acquisition, J.-I.H. All authors have read and agreed to the published version of the manuscript.

Data Availability Statement: Upon reasonable request, the corresponding author will provide the data reported in this work.

Conflicts of Interest: There are no conflicts of interest as declared by the authors. The design of the study; the collection, analyses, or interpretation of data; the writing of the manuscript; or the decision to publish the results, were all made without the input of the funders.

References

1. Mawuse, A.A.; Jeon-In, H. Chemically lithiated layered VOPO$_4$ by a microwave-assisted hydrothermal method and its electrochemical properties in rechargeable Li-ion batteries and supercapacitor applications. *J. Alloys Compd.* **2022**, *911*, 165067.
2. Guo, Y.; Wei, Y.; Shu, L.; Li, A.; Zhang, J.; Wang, R. Structure related RuSe$_2$ nanoparticles and their application in supercapacitors. *Colloids Surf. A Physicochem. Eng. Asp.* **2022**, *651*, 129702. [CrossRef]
3. Yan, B.; Feng, L.; Zheng, J.; Zhang, Q.; Jiang, S.; Zhang, C.; Ding, Y.; Han, J.; Chen, W.; He, S. High performance supercapacitors based on wood-derived thick carbon electrodes synthesized via green activation process. *Inorg. Chem. Front.* **2022**, *9*, 6108. [CrossRef]
4. Maria, R.L.; Bruce, D.; Yury, G. Multidimensional materials and device architectures for future hybrid energy storage. *Nat. Commun.* **2016**, *7*, 12647.
5. Sun, P.; Huang, J.; Xu, F.; Xu, J.; Lin, T.; Zhao, W.; Dong, W.; Huang, F. Boron-induced nitrogen fixation in 3D carbon materials for supercapacitors. *ACS Appl. Mater. Interfaces* **2020**, *12*, 28075–28082. [CrossRef]
6. Achal, S.K.; Prashant, D. Amorphous MnO$_x$ nanostructure/multiwalled carbon nanotube composites as electrode materials for supercapacitor application. *ACS Appl. Nano Mater.* **2022**, *5*, 8566–8582.
7. Zhai, Y.; Dou, Y.; Zhao, D.; Fulvio, P.F.; Mayes, R.T.; Dai, S. Carbon materials for chemical capacitive energy storage. *Adv. Mater.* **2011**, *23*, 4828–4850. [CrossRef]
8. Yan, B.; Zheng, J.; Wang, F.; Zhao, L.; Zhang, Q.; Xu, W.; He, S. Review on porous carbon materials engineered by ZnO templates: Design, synthesis and capacitance performance. *Mater. Des.* **2021**, *201*, 109518. [CrossRef]
9. Zheng, S.; Zhang, J.; Deng, H.; Du, Y.; Shi, X. Chitin derived nitrogen-doped porous carbons with ultrahigh specific surface area and tailored hierarchical porosity for high performance supercapacitors. *J. Bioresour. Bioprod.* **2021**, *6*, 142–151. [CrossRef]
10. Dhruba, P.C.; Arun, K.N. A review on the recent advances in hybrid supercapacitors. *J. Mater. Chem. A* **2021**, *9*, 15880.
11. Zhang, Q.; Yan, B.; Feng, L.; Zheng, J.; You, B.; Chen, J.; Zhao, X.; Zhang, C.; Jiang, S.; He, S. Progress in the use of organic potassium salts for the synthesis of porous carbon nanomaterials: Microstructure engineering for advanced supercapacitors. *Nanoscale* **2022**, *14*, 8216. [CrossRef] [PubMed]
12. Wei, L.; Deng, W.; Li, S.; Wu, Z.; Cai, J.; Luo, J. Sandwich-like chitosan porous carbon spheres/MXene composite with high specific capacitance and rate performance for supercapacitors. *J. Bioresour. Bioprod.* **2022**, *7*, 63–72. [CrossRef]
13. Feng, L.; Yan, B.; Zheng, J.; Chen, J.; Wei, R.; Jiang, S.; Yang, W.; Zhang, Q.; He, S. Soybean protein-derived N, O co-doped porous carbon sheets for supercapacitor application. *New J. Chem.* **2022**, *46*, 10844. [CrossRef]
14. Xu, J.; Xu, F.; Qian, M.; Xu, F.; Hong, Z.; Huang, F. Conductive carbon nitride for excellent energy storage. *Adv. Mater.* **2017**, *29*, 1701674. [CrossRef] [PubMed]
15. Qi, X.; Lin, T.; Zhang, S.; Xu, J.; Zhang, H.; Xu, F.; Huang, F. Nitrogen doped hierarchical porous hard carbon derived from a facial Ti-peroxy-initiating in-situ polymerization and its application in electrochemical capacitors. *Microporous Mesoporous Mater.* **2020**, *294*, 109884. [CrossRef]
16. Yang, X.; He, X.; Li, Q.; Sun, J.; Lei, Z.; Liu, Z.-H. 3D hierarchical NiCo$_2$S$_4$ nanoparticles/carbon nanotube sponge cathode for highly compressible asymmetric supercapacitors. *Energy Fuels* **2021**, *35*, 3449–3458. [CrossRef]
17. Dasha, K.K.; Anil, K.Y.; Hee, J.K. Hierarchical NiCo$_2$S$_4$ nanostructure as highly efficient electrode for high-performance supercapacitor applications. *J. Energy Storage* **2020**, *31*, 101619.

18. Wei, L.; Wu, Q.; Li, J. Review of NiCo$_2$S$_4$ nanostructures and their composites used in supercapacitors. *J. Mater. Sci. Mater. Electron.* **2021**, *32*, 12966–12990. [CrossRef]

19. Li, X.; Li, Q.; Wu, Y.; Rui, M.; Zeng, H. Two-dimensional, porous nickel-cobalt sulfide for high-performance asymmetric supercapacitors. *ACS Appl. Mater. Interfaces* **2015**, *7*, 19316–19323. [CrossRef]

20. Chen, T.; Wei, S.; Wang, P.Z. NiCo$_2$S$_4$ composite materials for supercapacitors. *ChemPlusChem* **2020**, *85*, 43–56. [CrossRef]

21. Kim, D.Y.; Ghodake, G.S.; Maile, N.C.; Kadam, A.A.; Lee, D.S.; Fulari, V.J.; Shinde, S.K. Chemical synthesis of hierarchical NiCo$_2$S$_4$ nanosheets like nanostructure on flexible foil for a high-performance supercapacitor. *Sci. Rep.* **2017**, *7*, 9764. [CrossRef]

22. Chen, H.; Jiang, J.; Zhang, L.; Wan, H.; Qi, T. Dandan Xia. Highly conductive NiCo$_2$S$_4$ urchin-like nanostructures for high-rate pseudocapacitors. *Nanoscale* **2013**, *5*, 8879–8883. [CrossRef]

23. Krishna, B.N.V.; Bhagwan, J.; Hussain, S.K.K.; Yu, J.S. Designing hierarchical NiCo$_2$S$_4$ nanospheres with enhanced electrochemical performance for supercapacitors. *J. Solid State Electrochem.* **2020**, *24*, 1033–1044. [CrossRef]

24. Chuai, M.; Zhang, K.; Chen, X.; Tong, Y.; Zhang, H.; Zhang, M. Effect of nondegeneracy on Ni$_{3-x}$Co$_x$S$_4$ for high performance supercapacitor. *Chem. Eng. J.* **2020**, *381*, 122682. [CrossRef]

25. Goli, N.; Sekhar, S.C.; Ramulu, B.; Yu, J.S. An integrated approach toward renewable energy storage using rechargeable Ag@Ni$_{0.67}$Co$_{0.33}$S-based hybrid supercapacitors. *Small* **2019**, *15*, 1805418.

26. Zhang, X.; Zheng, Y.; Zhou, J.; Zheng, W.; Chen, D. Nitrogen doped graphite felt decorated with porous Ni$_{1.4}$Co$_{1.6}$S$_4$ nanosheets for 3D pseudocapacitor electrodes. *RSC Adv.* **2017**, *7*, 13406. [CrossRef]

27. Ismail, M.M.; Hong, Z.Y.; Arivanandhan, M.; Yang, T.C.K.; Pan, G.T.; Huang, C.M. In situ binder-free and hydrothermal growth of nanostructured NiCo$_2$S$_4$/Ni electrodes for solid-state hybrid supercapacitors. *Energies* **2021**, *14*, 7114. [CrossRef]

28. Yang, Z.; Zhu, X.; Wang, K.; Ma, G.; Chen, H.; Xu, F. Preparation of NiCo$_2$S$_4$ flaky arrays on Ni foam as binder-free supercapacitor electrode. *Appl. Surf. Sci.* **2015**, *347*, 690–695. [CrossRef]

29. Wen, Y.; Liu, Y.; Wang, T.; Wang, Z.; Zhang, Y.; Wu, X.; Chen, X.; Peng, S.; He, D. High-mass-loading Ni-Co-S electrodes with unfading electrochemical performance for supercapacitors. *ACS Appl. Energy Mater.* **2021**, *4*, 6531–6541. [CrossRef]

30. Xue, Y.; Liu, X.; Han, L.; Xie, Z.; Liu, L.; Li, Y.; Hua, Y.; Wang, C.; Zhao, X.; Liu, X. Fabrication of hierarchical NiCo$_2$S$_4$ nanotubes@NiMn-LDH nanosheets core-shell hybrid arrays on Ni foam for high-performance asymmetric supercapacitors. *J. Alloys Compd.* **2022**, *900*, 163495. [CrossRef]

31. Zhao, H.; Li, F.; Wang, S.; Guo, L. Wet chemical synthesis of amorphous nanomaterials with well-defined morphologies. *Acc. Mater. Res.* **2021**, *2*, 804–815. [CrossRef]

32. Long, C.; Zheng, M.; Xiao, Y.; Lei, B.; Dong, H.; Zhang, H.; Hu, H.; Liu, Y. Amorphous Ni-Co binary oxide with hierarchical porous structure for electrochemical capacitors. *ACS Appl. Mater. Interfaces* **2015**, *7*, 24419–24429. [CrossRef]

33. Sun, R.; Gao, J.; Wu, G.; Liu, P.; Guo, W.; Zhou, H.; Ge, J.; Hu, Y.; Xue, Z.; Li, H.; et al. Amorphous metal oxide nanosheets featuring reversible structure transformations as sodium-ion battery anodes. *Cell Rep. Phys. Sci.* **2020**, *1*, 100118. [CrossRef]

34. Ren, L.L.; Wang, L.H.; Qin, Y.F.; Li, Q. One-pot synthesized amorphous cobalt sulfide with enhanced electrochemical performance as anodes for lithium-ion batteries. *Front. Chem.* **2021**, *9*, 818255. [CrossRef]

35. Zhou, X.; Gao, P.; Sun, S.; Bao, D.; Wang, Y.; Li, X.; Wu, T.; Chen, Y.; Yang, P. Amorphous, crystalline and crystalline/amorphous selenium nanowires and their different (de) lithiation mechanisms. *Chem. Mater.* **2015**, *27*, 6730–6736. [CrossRef]

36. Agyeman, D.A.; Park, M.; Kang, Y.M. Pd-impregnated NiCo$_2$O$_4$ nanosheets/porous carbon composites as a free-standing and binding-free catalyst for a high energy lithium-oxygen battery. *J. Mater. Chem. A* **2017**, *5*, 22234. [CrossRef]

37. Cao, W.; Chen, N.; Zhao, W.; Xia, Q.; Du, G.; Xiong, C.; Li, W.; Tang, L. Amorphous P-NiCoS@C nanoparticles derived from P-doped NiCo-MOF as electrode materials for high-performance hybrid supercapacitors. *Electrochim. Acta* **2022**, *430*, 141049. [CrossRef]

38. Yan, B.; Zheng, J.; Feng, L.; Du, C.; Jian, S.; Yang, W.; Wu, Y.A.; Jiang, S.; He, S.; Chen, W. Wood-derived biochar as thick electrodes for high-rate performance supercapacitors. *Biochar* **2022**, *4*, 50. [CrossRef]

39. Yan, B.; Feng, L.; Zheng, J.; Zhang, Q.; Dong, Y.; Ding, Y.; Yang, W.; Han, J.; Jiang, S.; He, S. Nitrogen-doped carbon layer on cellulose derived free-standing carbon paper for high-rate supercapacitors. *Appl. Surf. Sci.* **2023**, *608*, 155144. [CrossRef]

40. Cheng, D.; Zhong, Q.; Wang, J.; Bu, Y. Amorphous core-shell nanoparticles as a highly effective and stable battery-type electrode for hybrid supercapacitors. *Adv. Mater. Interfaces* **2019**, *6*, 1900858. [CrossRef]

41. Wen, Y.; Peng, S.; Wang, Z.; Hao, J.; Qin, T.; Lu, S.; Zhang, J.; He, D.; Fan, X.; Cao, G. Facile synthesis of ultrathin NiCo$_2$S$_4$ nano-petals inspired by blooming buds for high-performance supercapacitors. *J. Mater. Chem. A* **2017**, *5*, 7144. [CrossRef]

42. Atin, P.; Shilpi, S.; Sreehari, K.S.; Shreyasi, C.; Manab, K.; Pulickel, M.A. Ternary metal sulfides as electrode materials for Na/K-ion batteries and electrochemical supercapacitor: Advances/challenges and prospects. *Adv. Energy Mater.* **2024**, 2401657.

43. Zheng, J.; Yan, B.; Feng, L.; Zhang, Q.; Zhang, C.; Yang, W.; Han, J.; Jiang, S.; He, S. Potassium citrate assisted synthesis of hierarchical porous carbon materials for high performance supercapacitors. *Diam. Relat. Mater.* **2022**, *128*, 109247. [CrossRef]

44. Amedzo-Adore, M.; Yang, J.; Han, D.; Chen, M.; Agyeman, D.A.; Zhang, J.; Zhao, R.; Kang, Y.M. Oxygen-deficient P2-Na$_{0.7}$Mn$_{0.75}$Ni$_{0.25}$O$_{2-x}$ cathode by a reductive NH$_4$HF$_2$ treatment for highly reversible Na-ion storage. *ACS Appl. Energy Mater.* **2021**, *4*, 8036–8044. [CrossRef]

45. Amedzo-Adore, M.; Han, J.I. Investigating the pseudo-capacitive properties of interlayer engineered VOPO$_4$ by organic molecule intercalation. *Ceram. Int.* **2022**, *48*, 26226–26232. [CrossRef]

46. Yan, B.; Zheng, J.; Feng, L.; Zhang, Q.; Han, J.; Hou, H.; Zhang, C.; Ding, Y.; Jiang, S.; He, S. Green H_2O_2 activation of electrospun polyimide-based carbon nanofibers towards high-performance free-standing electrodes for supercapacitors. *Diam. Relat. Mater.* **2022**, *130*, 109465. [CrossRef]
47. Yang, J.H.; Shin, J.Y.; Amedzo-Adore, M.; Lau, V.W.H.; Yamauchi, Y.; Kang, Y.M. p-Phenylenediamine functionalization induced 3D microstructure formation of reduced graphene oxide for the improved electrical double layer capacitance in organic electrolyte. *ChemistrySelect* **2018**, *3*, 7680–7688. [CrossRef]